

1 A Machine Learning Methodology for the Generation of a Parameterization of the Hydroxyl Radical

2
3 Daniel C. Anderson^{1,2}, Melanie B. Follette-Cook^{2,3}, Sarah A. Strode^{2,3}, Julie M. Nicely^{2,4}, Junhua Liu^{2,3},
4 Peter D. Ivatt^{2,4}, Bryan N. Duncan²

5
6 ¹GESTAR II, University of Maryland Baltimore County, Baltimore, MD, USA

7 ²Atmospheric Chemistry and Dynamics Laboratory, NASA Goddard Space Flight Center, Greenbelt, MD,
8 USA

9 ³GESTAR II, Morgan State University, Baltimore, MD, USA

10 ⁴Earth System Science Interdisciplinary Center, University of Maryland, College Park, MD, USA

11
12 *Correspondence to:* Daniel C. Anderson (daniel.c.anderson@nasa.gov)

13 Abstract

14 We present a methodology that uses gradient boosted regression trees (a machine learning
15 technique) and a full-chemistry simulation (i.e., training dataset) from a chemistry climate model (CCM)
16 to efficiently generate a parameterization of tropospheric hydroxyl radical (OH) that is a function of
17 chemical, dynamical, and solar irradiance variables. This surrogate model of OH is designed to be
18 integrated into a CCM and allow for computationally-efficient simulation of nonlinear feedbacks
19 between OH and tropospheric constituents that have loss by reaction with OH as their primary sinks
20 (e.g., carbon monoxide (CO), methane (CH₄), volatile organic compounds (VOCs)). Such a model
21 framework is advantageous for studies that require multi-decadal simulations of CH₄ or multi-year
22 sensitivity simulations to understand the causes of trends and variations of CO and CH₄. To allow the
23 user to easily target the training dataset towards a desired application, we are outlining a methodology
24 to generate a parameterization of OH and not presenting an “off the shelf” version of a
25 parameterization to be incorporated into a CCM. This provides for the relatively easy creation of a new
26 parameterization in response to, for example, changes in research goals or the underlying CCM
27 chemistry and/or dynamics schemes. We show that a sample parameterization of OH generated from a
28 CCM simulation is able to reproduce OH concentrations with a normalized root mean square error of
29 approximately 5%, as well as capturing the global mean methane lifetime within approximately 1%. Our
30 calculated accuracy of the parameterization assumes inputs being within the bounds of the training
31 dataset. Large excursions from these bounds will likely decrease the overall accuracy. However, we
32 show that the sample parameterization predicts large deviations in OH for an El Niño event that was not
33 part of the training dataset, and that the spatial distribution and strength of these deviations are
34 consistent with the event. This result gives confidence in the fidelity of a parameterization developed
35 with our methodology to simulate the spatial and temporal responses of OH to perturbations from large
36 variations in the chemical, dynamical, and solar irradiance drivers of OH. In addition, we discuss how
37 two machine learning metrics, Gain feature importance and SHAP values, indicate that the behavior of a
38 parameterization of OH generally accords with our understanding of OH chemistry, even though there
39 are no physics- or chemistry-based constraints on the parameterization.

40 41 1.0 Introduction

42 The hydroxyl radical (OH) is the dominant tropospheric oxidant. It removes numerous species from
43 the atmosphere, including carbon monoxide (CO) and methane (CH₄), which are the largest OH sinks on
44 a global scale (Spivakovsky et al., 2000; Spivakovsky et al., 1990). Recent trends in CH₄, the second most
45 important anthropogenic greenhouse gas, can potentially be explained by changes in OH abundance
46 (Rigby et al., 2017), although changes in emissions are also a likely contributor (Turner et al., 2017).

47 Likewise, the large increase in CH₄ during 2020 has been attributed to decreases in OH resulting from
48 COVID-19 related changes in NO_x (NO_x = NO + NO₂) abundance (Laughner et al., 2021). Understanding
49 the non-linear chemistry of the drivers of OH and feedbacks among these species is therefore important
50 for characterizing past and present changes in the atmosphere as well as in projecting future climate
51 scenarios.

52
53 Chemistry-climate models (CCMs) with detailed chemical mechanisms are used to investigate the
54 complex, non-linear chemistry between these species and their impacts on the atmosphere (e.g., Fiore et
55 al., 2006; Voulgarakis et al., 2015; Gaubert et al., 2017; Holmes, 2018). The utility of CCMs for this
56 purpose is limited, however, by the large computational expense of a CCM with a full representation of
57 O₃ – NO_x – VOC (Ozone, NO_x, Volatile Organic Compound) chemistry combined with the need to model
58 over decadal time scales in order to let CH₄ perturbations fully evolve (Prather, 1996). Because of this
59 computational expense, simulations are necessarily limited to a short time frame, performed at coarse
60 horizontal resolutions, and/or limited in the number of sensitivity runs that can be performed (e.g., Fiore
61 et al., 2006; Holmes, 2018; Voulgarakis et al., 2015).

62
63 There are several alternatives (i.e., surrogate models) to running a full chemical mechanism that
64 capture some of the relationship between OH and trace gases, such as CO and CH₄, and are less
65 computationally expensive. Prescribed OH fields, either static or annually-varying, from a full chemistry
66 simulation or a climatology have been used for decades to simulate and understand trends in CO and
67 CH₄ in a computationally-efficient way (e.g., Saito et al., 2013; Wang et al., 2004). However, this method
68 linearizes CO and CH₄ chemistry with OH, preventing the simulation of nonlinear feedbacks in changes in
69 CO and CH₄ on OH, and thus could bias, for instance, interannual CH₄ changes (Chen and Prinn, 2006).

70
71 For over thirty years, parameterizations of OH have provided a viable alternative to climatologies in
72 helping to understand OH/CO/CH₄ feedbacks. Spivakovsky et al. (1990) developed a parameterization of
73 OH, later updated by Duncan et al. (2000), that captures many of the nonlinear feedbacks between OH
74 and tropospheric constituents (e.g., CO, CH₄, VOCs) that have loss by reaction with OH as their primary
75 sinks. The method to generate the parameterization uses higher order polynomials with various
76 chemical species, meteorological variables, and variables related to solar irradiance as inputs. The
77 degree of the nonlinear impacts simulated by the parameterization of OH depends on the method used
78 to populate these inputs. For instance, many of the meteorological and solar irradiance variables may be
79 provided by the model at run time. The chemical variables that are not all simulated explicitly in the
80 surrogate model may be provided as climatological or monthly means from a full chemistry simulation.
81 Duncan et al. (2007a) and Duncan and Logan (2008) used this parameterization of OH in an atmospheric
82 model of CO to elucidate the causes of trends and interannual variations in CO from 1988-1997 on
83 regional to global scales as well as those observed by individual *in situ* monitors around the world.

84
85 Building on the CO-OH studies of Duncan et al. (2007a) and Duncan and Logan (2008), Elshorbany et
86 al. (2016) developed the computationally Efficient CH₄-CO-OH (ECCOH) chemistry module, which
87 captures many of the nonlinearities and feedbacks of the CH₄-CO-OH system without the computational
88 expense of a full chemistry simulation. ECCOH calculates 24-hour averaged OH from a combination of
89 archived (e.g., multiple VOCs, NO_x) and online (e.g., pressure, temperature, cloud albedo) chemical,
90 meteorological, and solar irradiance variables. Despite the partial reliance of the parameterization of
91 OH in ECCOH on archived fields, its strength lies in the ability to calculate OH at a significantly reduced
92 computational expense (Duncan et al., 2000; Elshorbany et al., 2016). ECCOH has been successfully
93 implemented in the NASA Goddard Earth Observing System (GEOS) general circulation model (GCM).

94

95 Through manipulation of the input parameters (i.e., chemical, meteorological, and solar irradiance
96 variables) to the parameterization of OH, as well as emissions and dynamics, ECCOH can produce
97 multiple, computationally cheap, sensitivity simulations that help deconvolve the causes of local to
98 global trends and variations in OH, CO, and CH₄. For example, Strode et al. (2015) used the ECCOH
99 module to investigate the effects of different model biases in GEOS on simulated OH. To do this, they
100 performed multiple sensitivity simulations, adjusting tropospheric water vapor, ozone, and NO_x to
101 match satellite observations, to understand the impacts on OH and CH₄ lifetime. Similarly, Elshorbany et
102 al. (2016) investigated the impacts of varying CH₄ and CO emissions on the growth rate of atmospheric
103 methane concentrations through multiple sensitivity runs. One limitation of ECCOH in the configuration
104 used in Strode et al. (2015) and Elshorbany et al. (2016), however, is the difficulty in updating the
105 parameterization to reflect advances in atmospheric chemistry.

106
107 Machine learning algorithms are one potential method to quickly and accurately generate a new
108 parameterization of OH, offering an advance over the methods used in Duncan et al. (2000) and
109 Spivakovsky et al. (1990). A variety of machine learning techniques, such as neural networks (Nicely et
110 al., 2017; Nicely et al., 2020; Kelp et al., 2020), ridge regression (Nowack et al., 2018), random forest
111 regression (Keller and Evans, 2019; Sherwen et al., 2019), and gradient boosted regression trees (GBRTs)
112 (Ivatt and Evans, 2020; Stirnberg et al., 2020) have been successfully used in atmospheric chemistry
113 applications. In particular, GBRT models (Elith et al., 2008; Chen and Guestrin, 2016) use an ensemble of
114 decision trees to predict the value of a target based on multiple inputs and have been used to predict
115 surface OH using a combination of satellite observations and output from 3-dimensional models (Zhu et
116 al., 2022). Decision trees are created sequentially, with each new tree minimizing a cost function based
117 on the results of the previous tree (Elith et al., 2008; Stirnberg et al., 2020). Unlike some other machine
118 learning algorithms, such as neural networks, regression tree methods have easily interpretable metrics
119 that help highlight the influence of the different input variables (Yan et al., 2016). These metrics can
120 help further understanding of the model behavior in ways other machine learning techniques cannot.
121 GBRT models are also relatively quick to generate and can capture the highly non-linear relationships
122 that describe tropospheric chemistry (Ivatt and Evans, 2020).

123
124 We present a new method for the efficient generation of a parameterization of OH using GBRTs and
125 a full chemistry simulation from a CCM, which serves as the training dataset. We illustrate our method
126 by generating a parameterization of OH for the ECCOH module (Elshorbany et al., 2016), which captures
127 many of the nonlinearities and feedbacks of the CH₄-CO-OH system, as implemented into the NASA
128 GEOS GCM. Our methodology allows for the parameterization to be easily and rapidly regenerated in
129 response to changes in, for instance, the underlying model chemical mechanism (e.g., updates to the
130 chemical rate constants or absorption cross-sections) or model dynamics, which affect many of the
131 variables that influence OH (e.g., Anderson et al., 2021). Likewise, the parameterization can be modified
132 to include new input variables. This represents a significant advance over previous, much more
133 laborious, methodologies to generate a parameterization of OH. Users can and should retrain the
134 parameterization with datasets that are appropriate for the intended application. That is, we are not
135 offering a parameterization for “off the shelf” use but a methodology by which a user can easily create a
136 parameterization suitable for their needs. In Section 2, we outline the methodology used to develop the
137 parameterization of OH, while in Section 3, we evaluate performance of the parameterization. Finally,
138 in Section 4, we summarize the results and discuss implications for scientific research.

139 140 **2.0 Description of the Methodology to Generate a Parameterization of OH**

141 In this section, we outline the methodology to generate a parameterization of OH that may be used
142 in research studies as discussed above. Specifically, we illustrate the methodology by describing the

143 creation of a sample parameterization of OH for the ECCOH module that predicts daily averaged OH. In
144 Section 2.1, we present the creation of the training dataset, and in Section 2.2, we outline the
145 methodology used to create the parameterization of OH.

147 **2.1 Creation of the Training Dataset for a Parameterization**

148 We created the training dataset using output from a 40-year (1980 -2019) GEOS CCM simulation,
149 consistent with our intent to integrate the parameterization into the ECCOH modeling framework. This
150 simulation, called MERRA2 GMI (<https://acd-ext.gsfc.nasa.gov/Projects/GEOSCCM/MERRA2GMI/>), was
151 run in replay mode (Orbe et al., 2017) with MERRA2 (Modern Era Retrospective analysis for Research
152 and Applications) meteorology (Gelaro et al., 2017) and the Global Modeling Initiative (GMI) chemical
153 mechanism (Duncan et al., 2007b;Strahan et al., 2007). Aerosols were calculated with the Goddard
154 Chemistry Aerosol Radiation and Transport (GOCART) module (Chin et al., 2002;Colarco et al., 2010).
155 The model was run at a resolution of c180 on the cubed sphere (approximately 0.625° longitude by 0.5°
156 latitude) with 72 vertical layers. In this analysis, we use only tropospheric output at daily and monthly
157 resolutions. The GMI chemical mechanism includes approximately 120 species and 400 reactions,
158 characterizing the photochemistry of the troposphere and stratosphere. Further simulation details,
159 including a description of the emissions, are available elsewhere (Anderson et al., 2021;Strode et al.,
160 2019).

161
162 We created a dataset of training targets, representing the full range of simulated OH values, for
163 each month. We generate parameterizations for each month instead of one, yearly parameterization to
164 increase computational efficiency of the generation of the parameterization. The spatiotemporal
165 variability in the abundance and emissions of OH drivers on the yearly scale would necessitate a far
166 larger dataset and more complicated sampling procedures to ensure representativeness of both OH and
167 the input variables. As demonstrated in Section 3.0, the adopted monthly approach accurately captures
168 OH while limiting the size of the training dataset.

169
170 We generated the training dataset using daily averaged data. For each day of a month, we divided
171 all simulated tropospheric OH concentrations from the 40-year simulation into 20 equally-sized
172 percentile bins (i.e., 0 – 5th percentile, 5th – 10th percentile, etc.). Then, we randomly selected 200,000
173 values from each bin, resulting in 4,000,000 training targets for each day of the month. We also
174 included the maximum and minimum OH values of the entire dataset to represent the full range of
175 values. We then combined training targets to form one large dataset with 120,000,000 values (for a 30-
176 day month), encompassing the full range of OH concentrations from each day of the month. To limit the
177 size of the training dataset, we then subsampled these targets, again randomly selecting 200,000 values
178 from equally-sized percentile bins of OH concentration. The procedure resulted in a dataset with
179 4,000,000 training targets that span all days within a given month. A schematic of this process is shown
180 in Figure S1. We omitted data from 4 years (1985, 1995, 2005, 2015) from the training dataset for
181 model evaluation and from an additional year, 2016, for an El Niño case study discussed in Section 3.3.
182 We also created a training dataset for monthly-averaged output, discussed in Sect. 4.0, using an
183 analogous process.

184
185 Finally, for each OH target, we extracted the inputs for the regression tree parameterization from
186 the MERRA2 GMI simulation from the corresponding model grid box. We list parameterization inputs in
187 Table 1. The parameterizations of Spivakovsky et al. (2000), Duncan et al. (2007a) and Elshorbany et al.
188 (2016), along with expert knowledge of OH chemistry, informed our choice of inputs. The relative
189 location of a particular OH target is indicated with the latitude and pressure variables. As discussed in
190 the next section, NO₂ serves as a sufficient proxy for the impact of NO_x and NO_y on OH, so NO₂ is the

191 only reactive nitrogen species included as an input parameter. For both ice and water cloud as well as
 192 aerosol optical depths, we include the optical depth above and below each datapoint as separate inputs.
 193 We use aerosol optical depth (AOD) at 550 nm, calculated from the GOCART aerosol module. We took
 194 all 27 inputs from the MERRA2 GMI simulation except surface UV albedo, which we took from the Ozone
 195 Monitoring Instrument (OMI) climatology of Kleipool et al. (2008).

197 **Table 1:** Inputs to the machine learning parameterization of OH. UV Albedo is the value at the surface. Cloud fraction
 198 is the fraction at a given model level. C4 & C5 alkanes are one input as they originate from a lumped variable in the
 199 GMI mechanism.

<i>Chemical Inputs</i>		<i>Meteorological/Radiative Inputs</i>	
NO ₂	Formaldehyde (HCHO)	Temperature	Stratospheric O ₃ Column
CO	Hydrogen peroxide (H ₂ O ₂)	Cloud Fraction	Aerosol Optical Depth above
CH ₄	Methyl hydroperoxide (CH ₃ OOH; MHP)	Latitude	Aerosol Optical Depth below
O ₃	Acetone (CH ₃ COCH ₃)	UV Albedo	Water Cloud Optical Depth above
Isoprene (C ₅ H ₈)	C4 & C5 Alkanes	Water Vapor	Water Cloud Optical Depth below
Propene (C ₃ H ₆)	Ethane (C ₂ H ₆)	Pressure	Ice Cloud Optical Depth above
Propane (C ₃ H ₈)		Solar Zenith Angle	Ice Cloud Optical Depth below

200
 201 While we have used the publicly-available MERRA2 GMI dataset to train the sample
 202 parameterization described in this manuscript, the training data could come from any simulation or
 203 combination of self-consistent simulations that has output of the variables outlined in Table 1. These
 204 training datasets could come from existing simulations, which would greatly reduce computational
 205 expense, or from a training dataset tailored for the purposes of a given study. Even though we use
 206 daily-averaged training data for ECCOH, a user could train the parameterization with a dataset at any
 207 temporal resolution in order to make the parameterization compatible with a specific modeling platform
 208 or research goal. As discussed later, the parameterization performs best when applied to
 209 photochemical environments analogous to those on which it was trained. Therefore, users should
 210 carefully ensure that the training dataset reasonably encompasses the full range of photochemical
 211 environments necessary for a given sensitivity test or experiment. For example, as we will discuss
 212 further in Section 4, because the MERRA2 GMI training dataset only covers 1980 – 2018, it is
 213 inappropriate to use this for an application exploring changes in CH₄ from the pre-industrial period to
 214 2100. Instead, a new training dataset covering that time period would be required.

216 2.2 Creation of the GBRT Parameterization

217 While other machine learning methods could likely produce parameterizations with similar
 218 performance as the one we describe here, we use GBRTs because of the speed in training a new
 219 parameterization, their accuracy, and the interpretability of the parameterization itself. We refer to the
 220 GBRT models as parameterizations to prevent confusion when referring to 3-dimensional models.

221 We used the XGBoost package (Chen and Guestrin, 2016) version 0.81 in Python version 3.6 to
 222 create 12 parameterizations of OH (one for each month), training the parameterizations on the MERRA2
 223 GMI datasets described in Sect. 2.1. Each parameterization outputs 24-hour averaged OH. For each
 224 month, we used 80% of the dataset (3.2 million datapoints) for model training and the remainder for
 225 model validation. In addition, as outlined in-depth in Sections 2.1 and 3.0, we also evaluated the model
 226 on 5 years of data not included in the model training. Increasing the size of the training dataset did not

227 improve model performance but did increase model training time, so the training set was restricted to a
228 size that represented the full ranges of OH values.

229
230 To maximize parameterization performance while also balancing the potential of overfitting, we
231 tuned hyperparameters, including the learning rate, the maximum tree depth, and the number of trees.
232 We chose hyperparameter values that minimized the parameterization normalized root mean square
233 error (NRMSE) (Eq. 1.) of the training dataset. In Eq. 1, N is the number of samples, y is the MERRA2 GMI
234 OH, \hat{y} is the parameterized OH, and IQR is the interquartile range of the dataset. We set the learning
235 rate, which controls the magnitude of change when adding a new tree, to 0.1, while we varied the
236 maximum tree depth and number of trees from 6 to 22 and from 10 to 150, respectively. For both
237 maximum tree depth and number of trees, NRMSE initially dropped significantly with increasing value,
238 representing sharp improvement in parameterization performance. NRMSE values eventually
239 plateaued, increasing parameterization runtime without noticeably improving performance. A
240 combination of a maximum tree depth of 18 and 100 trees balanced performance with model training
241 and run time.

$$242 \quad NRMSE = \frac{\sqrt{\frac{1}{N} \sum_{i=1}^N (\hat{y}_i - y_i)^2}}{IQR} \quad (1)$$

243 We also evaluated inputs into the parameterization to ensure that each did not lead to decreased
244 performance, finding that no single variable dominates model performance and no variable reduces
245 performance. We retrained the parameterization 27 times for July, removing each input successively, to
246 determine its impact on the NRMSE. When we applied the resultant models to the July 2005 validation
247 dataset, the percentage change in the NRMSE generally increased by less than 1%. The small differences
248 in NRMSE indicate that there are likely variables that provide duplicate information to the
249 parameterization. As will be discussed in Sect. 3.2, however, the relative importance of inputs varies by
250 month, and some variables, though not important on average, have a large influence in specific chemical
251 environments. Because of these factors and a desire to use a consistent set of input variables across all
252 months, we did not remove any inputs from the parameterization as a result of this analysis.

253
254 Finally, we omit NO_x and NO_y as parameterization inputs because we find that NO_2 is sufficient as an
255 input to capture the impact of reactive nitrogen on OH in the parameterization. Because of the
256 importance of NO_x in OH production (Spivakovsky et al., 2000; Anderson et al., 2021), we tested
257 performance by substituting different reactive nitrogen species for NO_2 as inputs to the
258 parameterization. We trained three additional parameterizations, including ones with NO_x , NO_y ($\text{NO}_y =$
259 $\text{NO} + \text{NO}_2 + \text{PAN} + 2\text{N}_2\text{O}_5 + \text{HNO}_3 + \text{alkyl nitrates}$), and the individual NO_y species. Parameterization
260 performance did not improve noticeably with the inclusion of NO_x or the individual NO_y species.
261 Including NO_y as a group actually decreased performance.

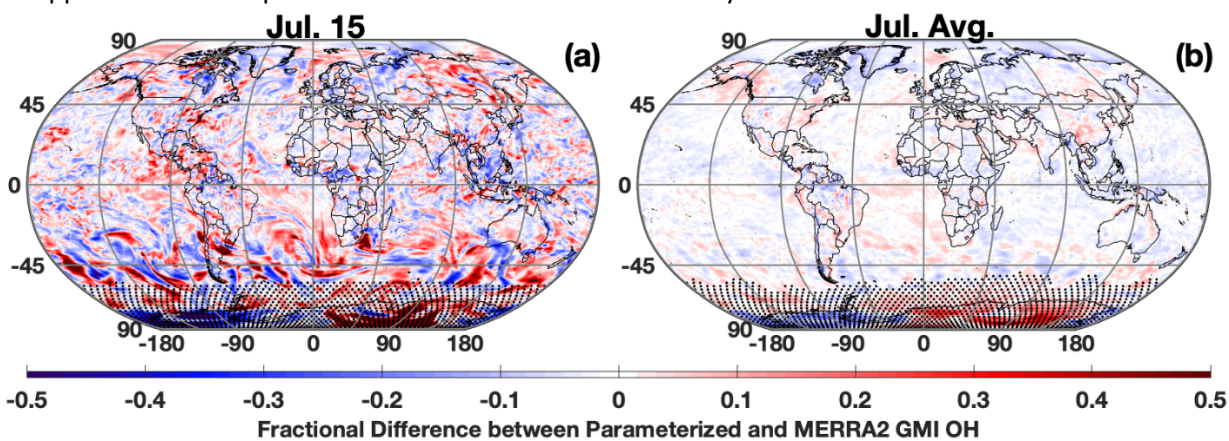
262 263 **3.0 Evaluation of the parameterization of OH for the ECCOH module**

264 We now evaluate the performance of the parameterization of OH for the ECCOH module created
265 with the machine learning methodology. In Section 3.1, we compare the OH calculated with the
266 parameterization to that from the MERRA2 GMI simulation, showing agreement in both local OH
267 concentrations as well as in global metrics, such as CH_4 lifetime (τ_{CH_4}). In Section 3.2, we investigate the
268 parameterization Gain feature importance and SHapley Additive Explanations (SHAP) values to
269 understand the relative contributions of inputs to parameterization performance and to demonstrate
270 that, even though there are no physics- or chemistry-based constraints, parameterization behavior
271 accords with our understanding of OH chemistry. We explore the ability of the parameterization to
272 predict OH in response to strong deviations in its drivers from the climatological mean in Section 3.3, by

273 examining two El Niño events. Finally, we note that we evaluate an offline version of the
274 parameterization of OH and not one integrated within the ECCOH framework. However, the
275 performance will be similar based on preliminary testing and similarities in implementation to the
276 previous parameterization, which has been extensively evaluated (Elshorbany et al., 2016) in the GEOS
277 GCM.
278

279 3.1 Ability of the parameterization to reproduce modeled OH and global OH metrics

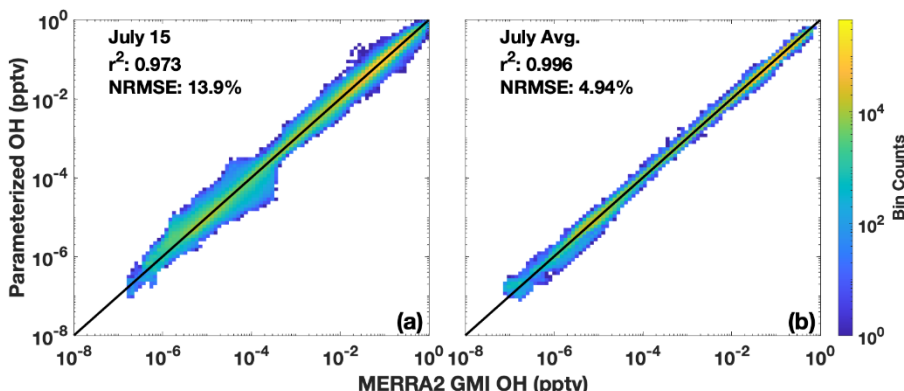
280 The parameterization is able to reproduce both the spatial distribution and concentration of
281 daily-averaged OH, although with noticeable errors at high latitudes in the winter hemisphere, which is
282 unimportant as OH is seasonally low. Figure 1a shows the fractional difference between OH calculated
283 with the parameterization and OH from the MERRA2 GMI simulation for July 15, 2005, a date omitted
284 from the training dataset. The parameterized and MERRA2 GMI OH fields are shown in Figure S2. The
285 OH in Figure 1 has been averaged over the lower free troposphere (LFT), defined as pressures between
286 the top of the planetary boundary layer (PBL) and 500 hPa. Agreement is similar throughout the
287 troposphere, but we highlight this region because of its importance for CH₄ and CO loss (Spivakovsky et
288 al., 2000). For July 15, there are notable regions of bias, particularly poleward of 30° S where OH is low
289 (Fig. S2). While the source of this error is unknown, it could result from a tendency of regression tree
290 models to have larger bias for lower values (Nowack et al., 2021). This results in a NRMSE for the entire
291 troposphere of 13.9% (Fig. 2a). At higher concentrations, the correlation between the MERRA2 GMI
292 simulation and the parameterized OH is much tighter than at lower concentrations, although the highest
293 density at all concentrations is centered around the 1:1 line. Because the CO and CH₄ lifetimes are much
294 longer than one day, the accuracy of the parameterization on monthly timescales is more relevant to
295 the applications of the parameterization than an individual day.



296 **Figure 1:** Fractional difference between the parameterized and MERRA2 GMI OH averaged over the LFT (top of the
297 PBL to 500 hPa) for July 15, 2005 (a) and averaged across all days for July 2005 (b). Regions with low OH, defined
298 as a mixing ratio of less than 0.005 pptv, are indicated with stippling.
299

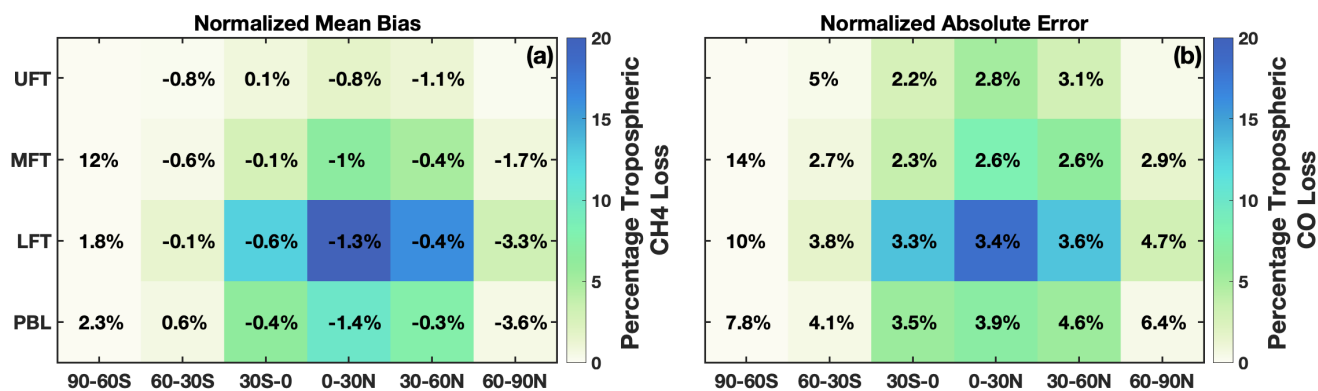
300 When we average the daily output to the monthly scale, the parameterization can reproduce
301 the global OH distribution with little error (Fig. 1-2). For July 2005, the percentage difference between
302 the parameterized OH and output from the MERRA2 GMI simulation in the LFT (Fig. 1b) and throughout
303 the troposphere (Fig. S3) is generally within 10%, outside of the Southern Hemispheric high latitudes,
304 where it is polar night and OH concentrations are negligible. The random errors evident in the daily data
305 in Figure 1a average out on the monthly timescale, resulting in a tight correlation ($r^2 = 0.996$) and a
306 NRMSE of 4.94% for all tropospheric values (Fig. 2b). Similar results are found for the July model when
307 applied to other years (Table S1) and for parameterizations developed for other months (Fig. S3 and S4).
308 Averaging the daily output over the monthly period yields a better NRMSE by more than a factor of two

309 over climatology (NRMSE = 11%), defined as the mean OH from the MERRA2 GMI simulation averaged
 310 over 1980 to 2019.
 311



312
 313 **Figure 2:** Scatter density plot of tropospheric OH from the MERRA2 GMI simulation plotted against OH calculated by
 314 the parameterization for July 15, 2005 (a). Panel (b) shows the 24-hour averaged OH output by the parameterization
 315 averaged across all July days for 2005. Colors indicate the number of data points in each bin. The r^2 of a linear least
 316 squares regression and the NRMSE are also indicated.
 317

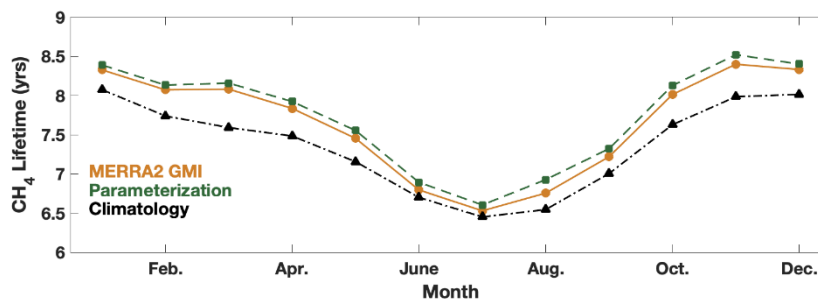
318 In regions where global CO and CH₄ loss are most important, parameterization biases and errors
 319 are low. For CO and CH₄, tropospheric loss to OH maximizes in the LFT in the 0 - 30° latitude band of the
 320 summer hemisphere with near negligible loss in the winter hemisphere polar region (Fig. 3). The
 321 comparatively large over- and underestimates over Antarctica evident in Figure 1 are irrelevant to the
 322 OH/CO/CH₄ cycle because of the low loss rate in this region. In contrast, in regions where CO and CH₄
 323 loss maximize, the parameterization is biased low by only -0.3 to -1.4%. The normalized absolute error
 324 varies between 2.2% and 4.6% in the tropics and Northern Hemispheric mid-latitudes for all
 325 tropospheric layers (MFT: pressures between 500 and 300 hPa, UFT: pressures between 300 hPa and the
 326 tropopause). Results are similar for other months.
 327



328
 329 **Figure 3:** (a) Percentage of total tropospheric CH₄ lost to reaction with OH for July 2005 averaged over 30° zonal
 330 mean bins and 4 atmospheric layers is shown by the background colors. The percentage loss values account for the
 331 mass of each region relative to the total atmospheric mass. Percentages indicate the normalized mean bias of the
 332 parameterization with respect to the MERRA2 GMI simulation. Statistics for the polar UFT are omitted because low
 333 tropopause heights limit the data amount in these regions. (b) Same as (a) except for tropospheric CO loss and the
 334 normalized absolute error.

335 The parameterization is also able to reproduce global mean metrics of OH, such as τ_{CH_4} , within
 336 1.3% on average. For each month of 2005, we calculated the global, mean mass-weighted tropospheric

337 OH as described in Lawrence et al. (2001) and the mean tropospheric τ_{CH_4} with respect to OH as
 338 described in Nicely et al. (2020) for the MERRA2 GMI simulation, the parameterization, and the
 339 climatological mean, defined as the average value from the MERRA2 GMI simulation between 1980 and
 340 2019. Results for τ_{CH_4} are shown in Figure 4, and for mass-weighted OH in Figure S5. The
 341 parameterization captures the seasonality of the τ_{CH_4} , with a minimum in boreal summer and a
 342 maximum in boreal winter. Agreement varies slightly by month, differing by only 0.8% in January and up
 343 to 2.5% in August, although the bias is systematically low for 2005 and the other validation years (Table
 344 S1). These values are reasonable and much smaller than the inter-model variability often seen in model
 345 intercomparison projects (e.g., Nicely et al., 2020; Voulgarakis et al., 2013). Similar results are found for
 346 the global, mean mass-weighted OH. The Northern Hemispheric/Southern Hemispheric OH ratio (Fig.
 347 S5) also generally agrees within 0.5% for all months, again with the exception of August. The
 348 comparatively weaker performance for August is limited to 2005, however, as performance of the
 349 August parameterization in the other validation years (1985, 1995, and 2015) is closer to the 1%
 350 difference shown by the parameterizations for the other months. The parameterizations present a
 351 significant improvement over the climatological mean, which for 2005, consistently underestimates τ_{CH_4}
 352 for all months and by up to 6% in March.
 353



354 **Figure 4:** Global mean methane lifetime with respect to tropospheric OH from the parameterization (green squares)
 355 and MERRA2 GMI (orange circles) for 2005 and the climatological average (black triangles) calculated from MERRA2
 356 GMI for 1980 - 2019.
 357

358 3.2 Understanding the relative importance of input parameters

359 While we have demonstrated that the parameterization is able to reproduce OH accurately, it is
 360 also instructive to understand the relative importance the parameterization places on each of the
 361 inputs. Although this parameterization is not process-based, understanding how the parameterization
 362 responds to different inputs can help determine if the regression tree is responding in a way consistent
 363 with current understanding of OH chemistry, although there are limitations to the information that can
 364 be gleaned from these metrics. We evaluate the regression tree parameterization using two metrics,
 365 the Gain feature importance as output by the XGBoost package, and SHAP values.
 366

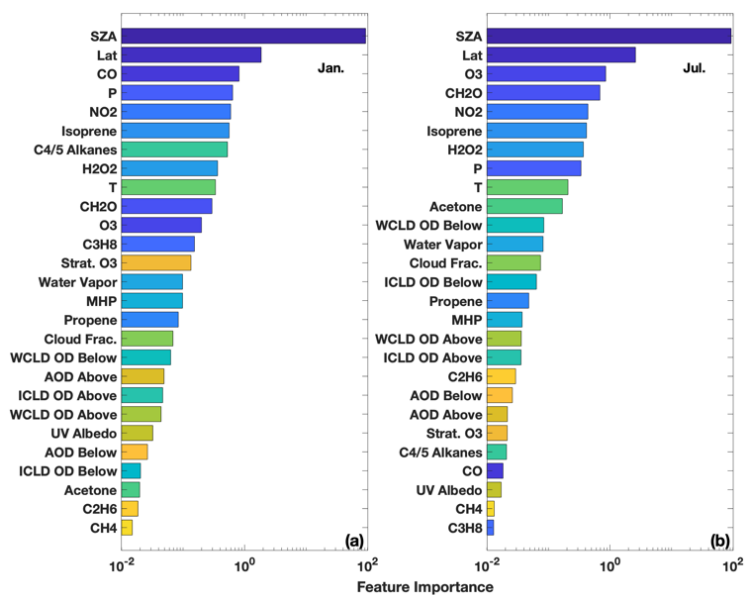
367 3.2.1 Investigating the Gain feature importance

368 The Gain feature importance (Chen and Guestrin, 2016) is a measure of the improvement in model
 369 accuracy achieved from adding branches in the model corresponding to a specific input variable. The
 370 Gain value therefore indicates the relative importance of each input for the model as a whole but not
 371 for individual datapoints. The Gain values for each input for the January and July models are shown in
 372 Figure 5. While there are differences between the two months, several features are similar. Variables
 373 that indicate geographic location (e.g., SZA, latitude, and pressure) and chemical species that have
 374 previously shown to be dominant drivers of OH variability (e.g., NO₂, O₃, CO) and/or OH proxies (e.g.,
 375 HCHO) (Wolfe et al., 2019; Murray et al., 2021) have some of the highest Gain values. As we show

376 below, caution should be used in extrapolating results from the Gain values to a process-based
 377 understanding of OH without prior knowledge of its response to chemical and dynamical drivers.

378
 379 The relative importance of variables that indicate location is consistent with OH chemistry and
 380 previous parameterization studies. Primary OH production is driven by the photolysis of O₃ followed by
 381 the subsequent reaction of the O¹D radical, produced from that photolysis, with water vapor (e.g.,
 382 Spivakovsky et al., 2000). Thus, the OH distribution is strongly dependent on SZA, latitude, and
 383 pressure. This is consistent with the parameterization, where SZA and latitude have the highest Gain
 384 values for both months examined here, as well as with the results of Duncan et al. (2000), who
 385 highlighted the importance of latitude in their parameterization.

386
 387 Similarly, the chemical species that are most important for controlling OH distribution on the global
 388 scale also tend to have higher Gain values. As discussed above, O₃ and NO_x chemistry is instrumental in
 389 controlling primary and secondary OH production on global scales (e.g., Spivakovsky et al.,
 390 2000; Anderson et al., 2021), consistent with their comparatively high Gain values. HCHO, an oxidation
 391 product of the reaction of OH with many VOCs, has been found to be a suitable proxy for OH in the
 392 remote atmosphere (Wolfe et al., 2019), consistent with its relative importance in both the July and
 393 January models.



394
 395 **Figure 5:** The feature importance (gains) of the January (a) and July (b) parameterizations as calculated by XGBoost.
 396 Variables are sorted by their relative importance. WCLD = Water cloud; ICLD = Ice Cloud; OD = Optical Depth.
 397 “Above” and “below” for the optical depth variables indicate the optical depth above and below a particular model
 398 grid box. Colors are assigned to the variables to permit easier comparison of the panels.

399
 400 The relative importance of global OH sinks in the parameterization, however, demonstrates the
 401 limitations of using the Gains values to interpret the regression tree model in a process-based way. CO,
 402 the dominant OH sink on a global scale (Spivakovsky et al., 2000), is the most important chemical input
 403 for the January parameterization, although it is relatively unimportant in the parameterizations for all
 404 other months. While tropical CO variability in MERRA2 GMI and biomass burning emissions (Duncan,
 405 2003b) are larger in boreal winter than July, there is no process-based explanation for why CO should be
 406 different in January from December or February. Differences in the relative importance of CO between
 407 the two months does not imply that OH sensitivity to CO in MERRA2 GMI or the atmosphere varies in

408 the same manner. Instead, the differences simply indicate that the parameterization algorithm finds CO
409 to be more useful in predicting OH in January than July. Similarly, CH₄, the second most important OH
410 sink on the global scale, has low Gain values, suggesting it has little impact on model performance. This
411 is likely because, in the MERRA2 GMI simulation, CH₄ concentrations vary little within a given latitude
412 band due to CH₄ surface concentrations being set as a boundary condition. The methane distribution
413 therefore provides little additional information beyond that already contained in the variables that
414 indicate location.

415

416 **3.2.2. Investigating parameterization SHAP values**

417 While the Gain values indicate the relative importance of species in the parameterization and can
418 provide some information as to whether the parameterization behaves in a manner consistent with our
419 understanding of OH chemistry, the metric only provides information about the dataset as a whole.
420 Gain values can therefore obscure the importance of variables that only strongly impact the
421 parameterization for a small subset of the data. To better understand the relative importance of
422 variables as well as the spatial variability in that importance, we also calculate the SHAP values
423 (Lundberg and Lee, 2017), which provide information on the relative importance of each datapoint input
424 into the model.

425

426 In the context of machine learning, Shapley values, an idea first developed for game theory
427 (Shapley, 1953), indicate the average contribution of an individual model input to all possible
428 combinations of inputs. For example, to calculate the Shapley value of the variable X for a hypothetical
429 machine learning model with three input variables X, Y, and Z, first a model would be trained with all
430 three variables. A new model would then be retrained, omitting X, and the difference between the two
431 models would be calculated to determine the contribution of X. This process would then be repeated
432 with different permutations of input variables (e.g., X and Y, X and Z) to determine the contribution of X
433 in those instances. The final Shapley value is the average of the contribution from these different
434 models. SHAP values use the same concept but in a manner that reduces the computation time
435 (Lundberg and Lee, 2017), as this process could become prohibitive for a model, such as the
436 parameterization of OH, that contains 27 inputs.

437

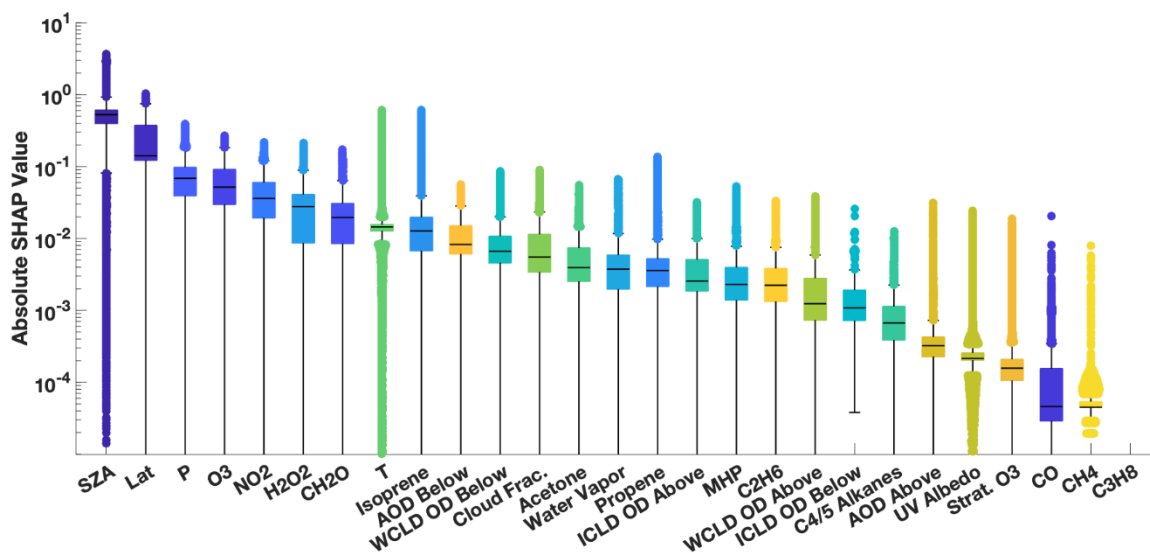
438 We calculate SHAP values using the TreeExplainer API of the SHAP package available for Python.
439 One limitation of the algorithm used to calculate SHAP values is that it is too computationally expensive
440 to calculate the SHAP values for the tuned regression tree model. Computational time to calculate SHAP
441 values for the troposphere at the native model resolution for one day is several months. Maximizing
442 computational speed by degrading the model resolution and running the SHAP package with GPUs,
443 would take approximately 4 days for one model day. Calculating SHAP values for a model with default
444 model hyperparameters, however, takes minutes. This is due to the large reduction in the number of
445 trees (100 to 10) and the maximum tree depth (18 to 6) in the parameterization, which significantly
446 speeds up the creation of new regression trees needed in the SHAP value calculation.

447

448 We first evaluate the feasibility of using the SHAP values for the untuned model to explain the
449 parameterization behavior. To test this, we created a subset of 5000 OH values from the
450 parameterization training dataset that spanned the full range of OH concentrations. We then calculated
451 the SHAP values for the July parameterization with tuned hyperparameters as well as for a July
452 parameterization using the default XGBoost hyperparameters. For the variables found to be most
453 important for the parameterization (e.g., SZA, NO₂, O₃, isoprene, HCHO, latitude), there are strong
454 correlations (r^2 of 0.97 or higher) for the SHAP values between the tuned and untuned model, resulting
455 in similar spatial distributions, although there are differences in the magnitude. For other variables,

456 correlation is much weaker, although the relative importance of variables is similar for the tuned and
457 untuned parameterizations. We therefore restrict our analysis primarily to variables that have highly
458 correlated SHAP values between the tuned and untuned models and discussion to the relative
459 importance of the different variables.
460

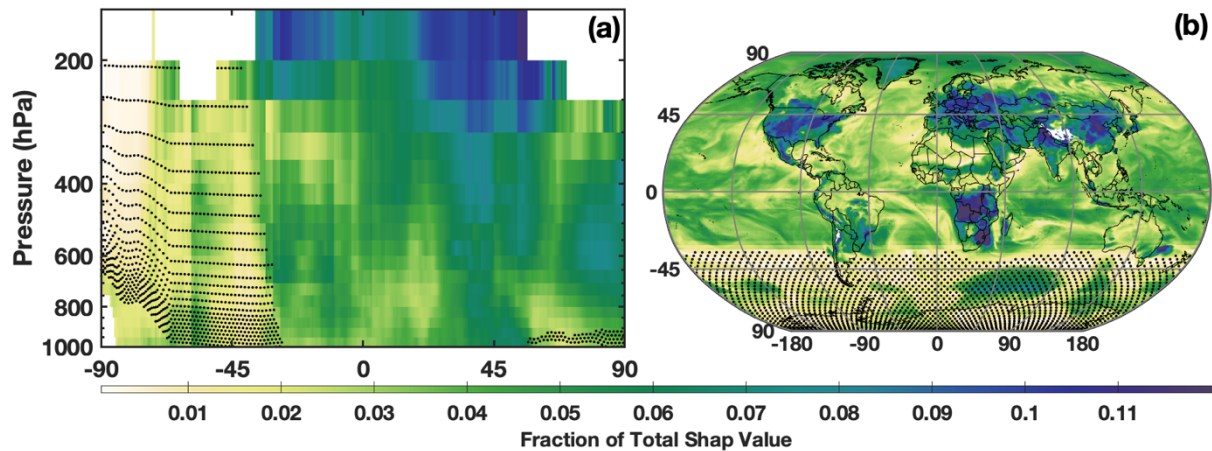
461 The distribution of SHAP values for the training dataset for July demonstrates the importance of
462 including each of the variables as inputs to the parameterization as well as the large variability in their
463 relative importance. Figure 6 shows the distribution of the SHAP values for each input parameter of the
464 approximately 3.2 million datapoints used to train the July parameterization. The median SHAP values
465 (Fig. 6) show similar ordering as the Gains feature importance (Fig. 5), with variables that indicate
466 location as well as O₃ and NO₂ being the most important in both cases. When looking at the distribution
467 of the SHAP values, however, it becomes apparent that variables that appear to be unimportant for
468 parameterization performance in the mean (e.g., propene and CH₄) can have large importance for
469 individual datapoints. For example, although propene can be locally important for OH chemistry, due to
470 its reactivity, concentrations in the remote atmosphere are low, making the species seem unimportant
471 in the aggregate. Similar results are found for the January parameterization (Fig. S6). As discussed in
472 Section 2.2, the SHAP values provide a rationale for including each of these species in the
473 parameterization.
474



475
476 **Figure 6:** Distribution of the absolute SHAP value for each parameterization input for July from an untuned version
477 of the parameterization of OH. Input parameters are sorted by order of relative importance. The median is indicated
478 with the black line, edges of the box represent the interquartile range, and whiskers represent the 5th and 95th
479 percentile. Values outside this range are indicated with circles. Note that the SHAP value for propane is zero,
480 indicating that it is not used by the untuned parameterization.

481
482 The SHAP values also demonstrate the spatial distribution of the relative importance of the
483 different chemical OH drivers. Figure 7 shows the relative importance of NO₂, as determined by the
484 SHAP values for the untuned parameterization, for both the zonal mean and the LFT. Note that the
485 untuned parameterization has large errors for low OH concentrations, so SHAP values poleward of 45 °S
486 should be viewed as more uncertain than those elsewhere. In both the horizontal and vertical, the SHAP
487 values demonstrate that the parameterization captures the spatial pattern of the relative importance of
488 NO_x for OH production. The spatial pattern in Figure 7a, for example, has the highest contribution of

489 NO₂ to the total SHAP value in the tropical UFT and in the northern hemisphere midlatitudes. This is
 490 nearly identical to the spatial pattern of the relative contribution of the NO + HO₂ reaction to overall OH
 491 production in the MERRA2 GMI simulation (Anderson et al., 2021). Likewise, in the LFT, the contribution
 492 from NO₂ maximizes over continental regions with high emission and minimizes over the remote oceans.
 493 The spatial pattern of SHAP values of isoprene also agree with OH chemistry, maximizing in regions of
 494 strong biogenic emissions and minimizing over oceans (Fig. S7). These SHAP values demonstrate that,
 495 although the parameterization is not process-based, its behavior at least partially accords with our
 496 understanding of OH chemistry.
 497



498
 499 **Figure 7:** The fraction of the contribution of the NO₂ SHAP value to the sum of the absolute SHAP value of all inputs
 500 in July is shown for the zonal mean (a) and the LFT (b). Regions where mean OH mixing ratios are below 0.03 pptv,
 501 the point below which the untuned parameterization is unable to reasonably predict OH, are indicated by the
 502 stippling.
 503

504 3.3 Case Study: Testing the parameterization response to the 2016 El Niño Event

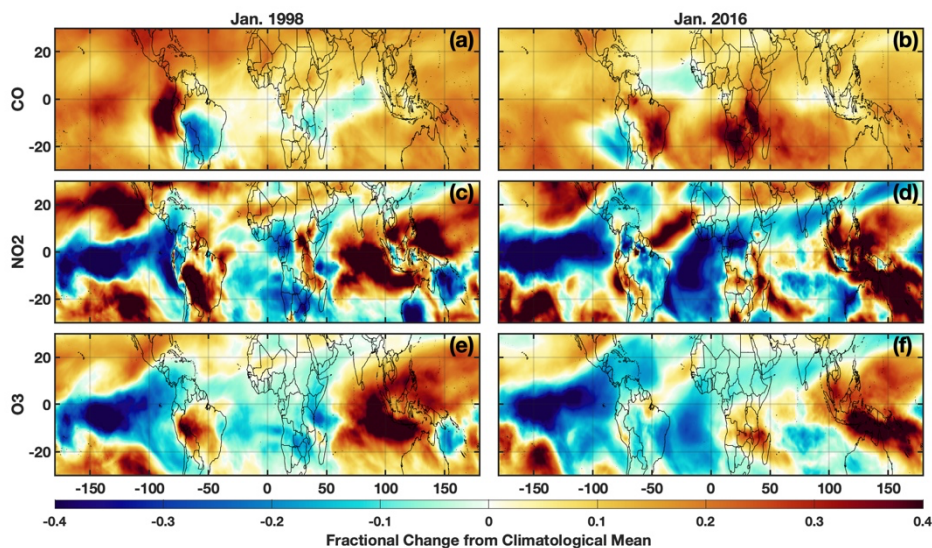
505 While we have demonstrated that the parameterization can satisfactorily reproduce OH during all
 506 months of 2005, we now investigate its ability to capture OH accurately during the 2016 El Niño event.
 507 which we excluded from the training dataset. Evaluating how the parameterization responds to
 508 deviations from the climatological mean of the inputs during a large-scale event on which it was not
 509 trained, such as the 2016 El Niño, is a strong test of its ability to predict extremes in OH as well as to
 510 respond to deviations from the climatological mean of the parameterization inputs. The response of the
 511 parameterized OH to these extremes in inputs will also provide a further test of the ability of the
 512 parameterization to behave in a process-based way.
 513

514 El Niño events lead to dramatic changes in the concentrations and distributions of many OH
 515 drivers, including O₃ (Oman et al., 2011;Oman et al., 2013), CO (Duncan, 2003a;Rowlinson et al., 2019),
 516 NO_x (Murray et al., 2013;Murray et al., 2014) and water vapor (Shi et al., 2018;Anderson et al., 2021).
 517 As such, the El Niño Southern Oscillation (ENSO) is the dominant mode of OH variability throughout
 518 much of the troposphere and can result in localized changes in OH on the order of 40 – 50% from the
 519 climatological mean (Anderson et al., 2021;Turner et al., 2018). Changes in secondary production from
 520 NO_x in the UFT and changes in primary production from O₃ in the PBL and LFT drive the ENSO related
 521 variability of OH (Anderson et al., 2021). Methane emissions also vary strongly with the ENSO phase
 522 (Zhang et al., 2018;Worden et al., 2013). In order to capture the OH/CH₄/CO system correctly, the
 523 parameterization must be able to capture ENSO-related OH variability.
 524

525 Here, we investigate the ability of the parameterization to capture OH during the El Niño events of
 526 1997/98 and 2015/16, two of the largest such events during the period of the MERRA2 GMI simulation
 527 according to the Multivariate ENSO Index (Wolter and Timlin, 2011). The 1997/98 event, which was
 528 included in the training dataset, was a prototypical example of an Eastern Pacific (EP) El Niño,
 529 characterized by sea surface temperature (SST) anomalies extending to the coast of South America. In
 530 contrast, the 2015/16 event was a blend of an EP and a Central Pacific (CP) El Niño, also known as El
 531 Niño Modoki, where SST anomalies extend only to the international dateline (Paek et al., 2017). These
 532 different “flavors” of El Niño affect atmospheric distributions of OH drivers, such as water vapor (Du et
 533 al., 2021), in different ways, suggesting different impacts on OH. While we did include other blended El
 534 Niños (1986/87, 1987/88, and 1991/92) (Kug et al., 2009) in the training dataset, each had responses in
 535 the atmospheric distribution of OH and its drivers distinct from the 2015/16 event. We focus our
 536 investigation on January and the MFT, the time and location of the strongest correlation between ENSO
 537 and OH (Anderson et al., 2021) in the MERRA2 GMI simulation. We also restrict the analysis to the OH
 538 precursors, NO₂, CO, and O₃, as they have both a strong influence in the variability of ENSO-related OH
 539 production/loss and have comparatively large feature importance and SHAP values in the January
 540 parameterization.

541
 542 For both the 1997/98 and 2015/16 El Niño events, each OH driver examined deviates strongly
 543 from the climatological mean, defined as the average value from the MERRA2 GMI simulation over all
 544 Januarys from 1980 – 2019. Both O₃ and NO₂ have pronounced positive anomalies over the western
 545 Pacific and maritime continent and negative anomalies over the eastern Pacific (Fig. 8) that extend
 546 throughout much of the free troposphere (Fig. S8), likely associated with changes in the Walker
 547 Circulation as described in Oman et al. (2011). The positive anomalies over Indonesia show a distinct
 548 westward shift during the 1997/98 event as compared to 2015/16, highlighting the variability in the
 549 effects of ENSO on emissions and transport. CO has a large positive anomaly over much of the globe,
 550 attributable to the increases in biomass burning during El Niño events (e.g., Duncan, 2003a). As with O₃
 551 and NO₂, there are large differences in the spatial pattern of the CO anomalies between the two events,
 552 particularly over the Indian Ocean, central Africa, and South America.

553



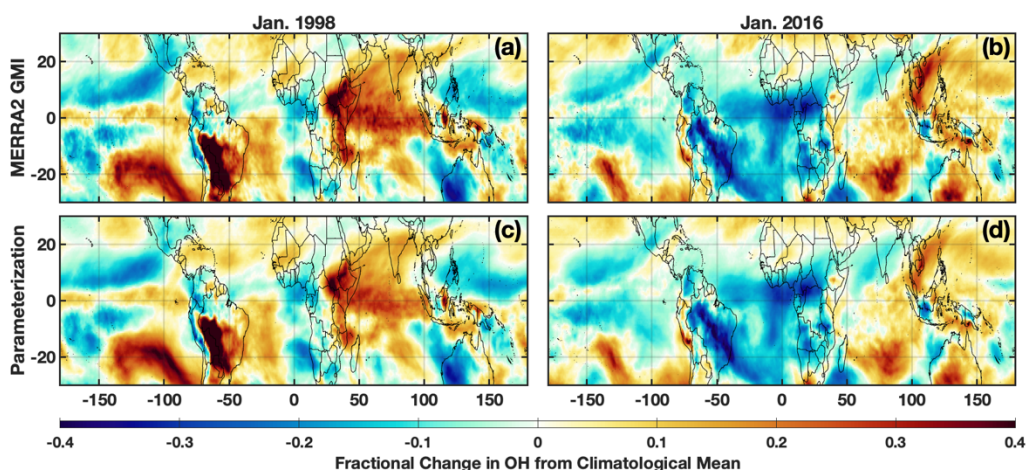
554 **Figure 8:** Fractional difference of the indicated variable between January 1998 (left) and the climatological mean
 555 (1980 – 2019) calculated from the MERRA2 GMI simulation for the MFT. The same values but for January 2016 are
 556 indicated on the right. Species shown are CO (a,b), NO₂ (c,d) and O₃ (e,f).
 557

558

559 The differences in anomalies of the OH drivers between the 1997/98 and 2015/16 El Niño events
 560 lead to distinct anomaly patterns in OH itself. During the 1997/98 event, in the MFT, there are
 561 noticeable positive anomalies in OH over much of the Indian Ocean basin, the southeastern Pacific,
 562 South America, and the western Atlantic Ocean (Fig. 9). During 2015/16, the positive anomalies were
 563 more limited and most noticeable in the tropical western Pacific Ocean and southern Indian Ocean.
 564 Along the equator, the positive anomalies extended throughout a larger portion of the troposphere
 565 during January 1998 than 2016. Both the parameterization inputs and the OH itself respond strongly
 566 and in different ways to each El Niño event, providing a strong test to determine the robustness of the
 567 parameterization.

568 The parameterization reproduces the ENSO-related OH anomalies for both El Niño events with
 569 remarkable fidelity. We ran the parameterization for all Januarys from 1980 to 2016 to calculate a
 570 climatology and calculated the deviations for 1998 and 2016 from that value. For both events, the
 571 parameterization accurately captures the location and magnitude, as well as the spatial pattern, of the
 572 OH anomalies with a few minor exceptions in the horizontal and vertical (Figs. 9 and S8). Correlation
 573 between the MERRA2 GMI and parameterized anomalies plotted in Figure 9 has an r^2 of 0.93 or higher
 574 for both years. The parameterization is therefore capable of reproducing both the climatological mean
 575 of OH as well as large deviations in the mean in response to strong climatological deviations in the
 576 model inputs, even for years excluded from the training dataset.

577



578 **Figure 9:** Fractional difference of the indicated variable between January 1998 (left) and the climatological mean
 579 (1980 – 2019) calculated from the MERRA2 GMI simulation averaged over the MFT. The same values but for January
 580 2016 are indicated on the right. Species shown are OH from the MERRA2 GMI simulation (a,b) and OH calculated by
 581 the parameterization (c,d).
 582

583 **4.0 Discussion and Summary: The parameterization of OH as a tool for scientific research**

584 In this manuscript, we present a new methodology to generate a parameterization of OH that, as
 585 compared to previous methods (e.g., Spivakovsky et al., 1990; Duncan et al., 2000), is efficient and easy
 586 to use, allowing the user to rapidly update the parameterization of OH as necessary. The new method
 587 uses GBRTs and a full-chemistry simulation from a CCM as the training data to generate the
 588 parameterization of OH with a high degree of accuracy relative to the full-chemistry simulation. We
 589 illustrated our methodology with a parameterization designed for the ECCOH module of the GEOS CCM.
 590

591 The parameterization of OH accurately reproduces OH from the full-chemistry simulation on
 592 which it was trained, but it may not produce the desired accuracy for a given time period or scenario
 593 outside the range represented in the training data. Of course, the degree of degradation in accuracy

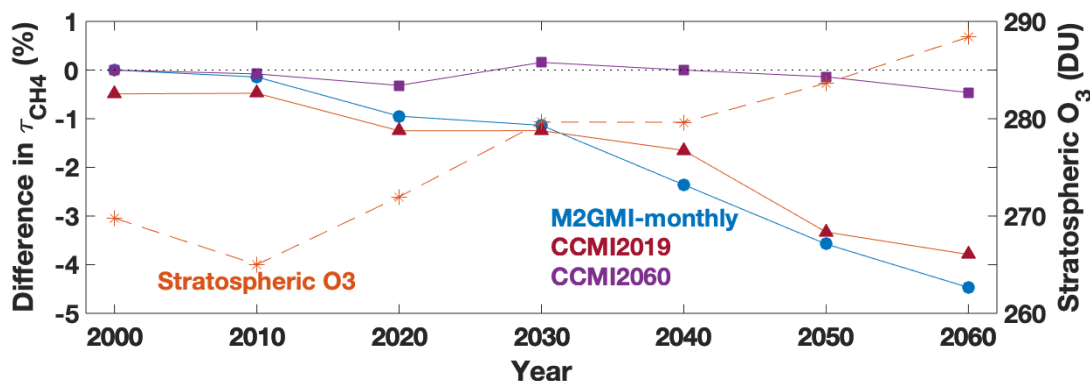
594 depends on how far inputs exceed the ranges of the training dataset. In addition, the parameterization
595 of OH generated using inputs from one model may not be portable to another model or even a different
596 configuration of the same model as shown below. The simulated relationships between OH and the
597 input parameters may differ because of inter-model variations in the chemical, dynamical, and radiative
598 schemes. Ultimately, it is up to the user to determine an acceptable level of degradation for a specific
599 research topic. In this section, we give an example of the degree of degradation in accuracy for a
600 parameterization of OH that uses 1) a different time period for the same model and 2) input parameters
601 from a different model.
602

603 **4.1: Input parameters from a different time period for the same model setup**

604 Analysis of a separate model simulation, the Chemistry Climate Model Initiative (CCMI) GEOS
605 simulation (Morgenstern et al., 2017), highlights possible limitations in extending the parameterization
606 to years outside of those on which it was trained, particularly if there is a strong trend in one of the
607 inputs. The GEOS CCMI simulation has unconstrained meteorology, spans 1960 – 2100, and has a
608 horizontal resolution of 2.0° latitude × 2.5° longitude. Emissions for precursors of tropospheric O₃ and
609 aerosols are from the RCP6.0 scenario. We trained two new parameterizations on the CCMI dataset,
610 denoted CCMI2019 and CCMI2060, using data from 1980 – 2019 and 1980 – 2061, respectively. We
611 used the same methodology to create the training datasets as for the MERRA2 GMI parameterization.
612 CCMI output are only available at monthly resolution, so we trained the CCMI parameterizations on
613 monthly, instead of daily, averaged values. Every 10th year, starting in 2000, was omitted from the
614 training dataset for validation.
615

616 While the CCMI2019 parameterization performed similarly to the MERRA2 GMI
617 parameterization for years included in the training dataset, performance degraded significantly for years
618 beyond 2019. The CCMI2019 parameterization captured the τ_{CH_4} for 2000 and 2010 within 1% (Fig. 10,
619 red line) and the NRMSE within 5% (not shown). When we applied the parameterization to years
620 outside of the training window, however, performance degraded quickly and, by 2060, underestimated
621 τ_{CH_4} by about 4%. The CCMI2060 parameterization, on the other hand, captures the τ_{CH_4} lifetime within
622 0.5% for all validation years.
623

624 The reason for this performance degradation is likely due to input parameters that extend
625 beyond the range used in the training dataset. For example, there is a strong positive trend in the
626 stratospheric O₃ column (Fig. 10), which results in chemical environments in 2060 that did not exist in
627 the 1980 – 2019 training dataset. Other variables with strong trends, such as CH₄ and temperature, as
628 well as different large-scale dynamical patterns, could also decrease parameterization performance.
629 These results strongly suggest caution when applying the parameterization to future scenarios outside
630 of the training window. As will be discussed in the following section, care should be taken in choosing
631 the training dataset to ensure that it represents the full range of photochemical conditions on which the
632 parameterization will be applied.
633



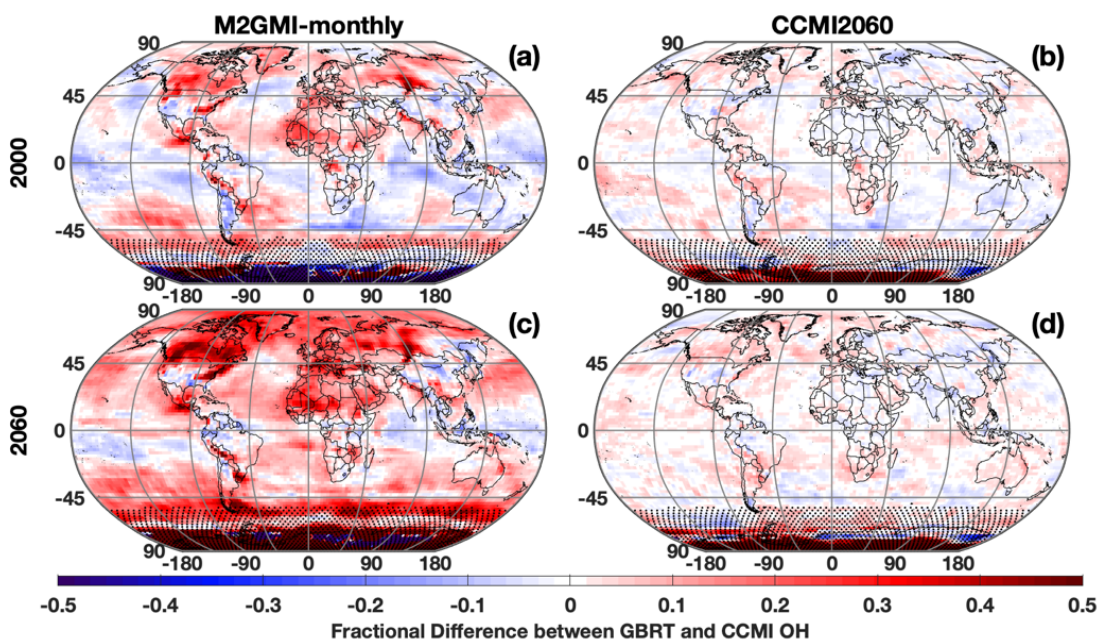
634
 635 **Figure 10:** Time series showing the percent difference between τ_{CH_4} calculated from the CCMI simulation and from
 636 three separate parameterizations: one trained on MERRA2 GMI output from 1980 – 2019 (blue circle), one trained
 637 on CCMI output spanning 1980 – 2019 (red triangle), and one trained on CCMI output spanning 1980 – 2060 (purple
 638 square). The stratospheric O_3 column (orange star) from the CCMI simulation averaged over 30 S to 60 N, the region
 639 where tropospheric CH_4 loss to OH maximizes (Fig. 3), is also shown. All data are for July.

640 4.2 Input parameters from a different model setup

641 Similar to applying the parameterization outside of the timeframe on which it was trained,
 642 applying the parameterization to a different model setup also warrants caution, as the differences can
 643 result in new chemical environments on which the parameterization was not trained. We now discuss
 644 parameterization performance when output from the CCMI simulation discussed in Section 4.1 is input
 645 into the MERRA2 GMI-trained parameterization. Despite both simulations being from the GEOS
 646 framework, the CCMI simulation setup differs from the MERRA2 GMI simulation in emissions, time
 647 frame, resolution, and meteorology (unconstrained vs specified dynamics), among others. Because
 648 CCMI output is only available at a monthly resolution, we created a separate parameterization,
 649 hereafter referred to as “M2GMI-monthly”, using MERRA2 GMI output with identical parameterization
 650 inputs as the daily parameterization but using monthly-averaged values. Performance is similar to that
 651 of the parameterization trained on daily data and averaged over monthly timescales, with the NRMSE
 652 for the troposphere on the order of 6 -7% depending on the year.

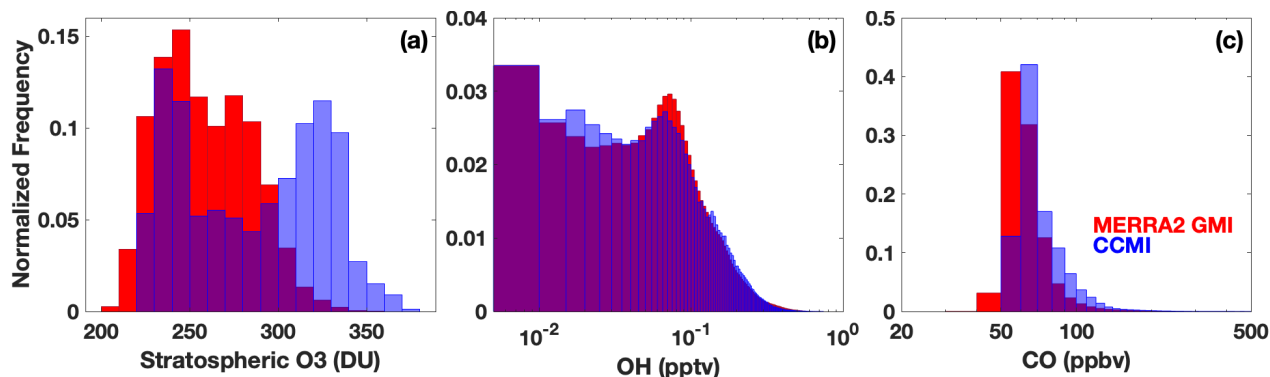
653
 654 When output from the CCMI simulation is used as inputs to the M2GMI-monthly
 655 parameterization, performance degrades significantly. For July 2000, for example, there are distinct
 656 regions of both positive and negative biases (Fig. 11a) in parameterized OH, resulting in a NRMSE of
 657 13%, on par with using climatology as an OH estimate. Because the largest discrepancies are centered
 658 outside of the tropics and/or in regions with low concentrations, τ_{CH_4} for year 2000 is identical between
 659 the CCMI and parameterized OH. When applied to 2060 (Fig. 11c), which is far outside the training
 660 period of the M2GMI-monthly parameterization, there is a near universal high bias in parameterized OH,
 661 resulting in a NRMSE of 16% and a τ_{CH_4} biased low by 4.5%. This overestimate results in a negative trend
 662 in τ_{CH_4} from parameterized OH from 2000 to 2060 (Fig. 10, blue line), despite the trend in the CCMI
 663 simulation being positive. Applying the MERRA2 GMI parameterization to a study using the CCMI setup
 664 would therefore misrepresent the OH/ CH_4 cycle.

665



666
 667 **Figure 11:** Fractional difference between OH calculated by the M2GMI-monthly (left) and the CCMI2060 (right)
 668 parameterizations and OH output from the CCMI simulation. Data are averaged between 850 and 500 hPa for July
 669 2000 (top) and July 2060 (bottom). Regions with low OH, defined as a mixing ratio of less than 0.005 pptv, are
 670 indicated with stippling.

671 Through an analysis of the ranges of input parameters from both simulations, we found that the
 672 differences in parameterization performance for inputs from MERRA2 GMI and CCMI are likely largely
 673 attributable to differences in the stratospheric O₃ distributions between the two simulations. In 2060,
 674 for example, CCMI stratospheric O₃ has a much higher frequency of values above 300 DU than the
 675 M2GMI-monthly training dataset (Fig. 12). A smaller, but still noticeable, shift in the distribution is also
 676 found for the year 2000 (Fig. S9). Likewise, the accuracy of the M2GMI-monthly parameterization
 677 decreases from 2000 – 2060 as the stratospheric O₃ burden increases (Fig. 10, red line). Mechanistically,
 678 higher stratospheric ozone in CCMI should result in lower tropospheric OH because the reduction in
 679 incoming ultraviolet radiation limits tropospheric O₃ photolysis. This could also lead to a higher CO
 680 burden, due to the smaller OH sink. Comparisons between the OH and CO distributions from the two
 681 simulations are consistent with this hypothesis. Even though the M2GMI-monthly training dataset
 682 spanned the full range of stratospheric O₃ values from the CCMI simulation, the frequency of
 683 stratospheric O₃ values at higher concentration likely creates chemical environments in the CCMI
 684 simulation distinct from those in MERRA2 GMI, forcing the parameterization to extrapolate to a
 685 chemical space on which it was not trained. This highlights the need to compare the distribution of any
 686 parameterization inputs to that of the training dataset to ensure that the training dataset fully
 687 encompasses the range of photochemical environments necessary for a given study. Once integrated
 688 into a modeling framework, safeguards could be added to warn a user if parameterization input values
 689 fall outside of the bounds of the training dataset, as is done with the current ECCOH parameterization.
 690



691
 692 **Figure 12:** Histograms showing the distribution of stratospheric column O₃ (a), tropospheric OH (b) and tropospheric
 693 CO (c) from the M2GMI-monthly parameterization training dataset (red) and from the CCMI simulation for 2060
 694 (blue). Purple indicates areas of overlap between the two distributions.

695 Again, performance improves significantly when we apply output from the CCMI simulation to the
 696 CCMI2060 parameterization. The regions of consistent high bias notable when CCMI output was applied
 697 to the M2GMI-monthly parameterization are absent for both 2000 and 2060, and NRMSE shows a factor
 698 of three improvement over the previously discussed scenario. Likewise, for all validation years, the
 699 parameterized OH resulted in a τ_{CH_4} that agreed with the CCMI simulation between 0 and -0.46% (purple
 700 line, Fig. 10).

701
 702 We conclude that for best performance, a separate parameterization should be created for each
 703 new modeling framework to capture OH variability accurately. This will not create an undue
 704 computational expense on an experiment. Because a full chemistry simulation is necessary to create the
 705 parameterization inputs of chemical species that are not calculated online, the necessary data to create
 706 a training dataset will already be available. The only additional time will be that required to format the
 707 regression tree inputs and to train the model, which takes approximately 2 – 3 hours for each month.
 708 This process can be performed using previously created python scripts with minimal changes. The
 709 flexibility that this modeling framework permits will facilitate its use even if there are major changes to
 710 the underlying model chemistry or dynamics.

711
 712 The methodology we present here allows for the quick generation of a parameterization of OH for
 713 use in a chemistry climate model to help disentangle the complicated relationship between CO, CH₄, and
 714 OH. The parameterization is designed for computationally inexpensive sensitivity runs and, as such, is
 715 not designed to capture feedbacks between OH and all of its chemical and dynamical drivers (e.g. H₂O₂
 716 or MHP). Instead, if a user is interested in these feedbacks, they could use the results of the sensitivity
 717 tests to identify times, locations, or chemical regimes for a targeted full chemistry simulation. Likewise,
 718 the parameterization reflects the photochemical environments of the dataset on which it was trained.
 719 Therefore, the training dataset should be carefully chosen to reflect the goals of a given study.
 720 However, we have demonstrated that the sample parameterization outlined here accurately predicts
 721 the magnitude and spatial distribution of the large deviations in OH for the 2016 El Niño, an event that
 722 was not part of the training dataset. This result gives confidence in the fidelity of a parameterization
 723 developed with our methodology to simulate the spatial and temporal responses of OH to perturbations
 724 from large variations in the chemical, dynamical, and solar irradiance drivers of OH.

725 726 **5.0 Code Availability**

727 The scripts used to create the training datasets and a sample script to create a parameterization have
 728 been archived by Zenodo at <https://doi.org/10.5281/zenodo.6046037> (Anderson, 2022a). A sample

729 parameterization for the ECCOH module trained on MERRA2-GMI output is available at
730 <https://doi.org/10.5281/zenodo.6604130> (Anderson, 2022b).

731

732 **6.0 Data Availability**

733 Output from the MERRA2 GMI simulation are publicly available at [https://acd-](https://acd-ext.gsfc.nasa.gov/Projects/GEOSCCM/MERRA2GMI/)
734 [ext.gsfc.nasa.gov/Projects/GEOSCCM/MERRA2GMI/](https://acd-ext.gsfc.nasa.gov/Projects/GEOSCCM/MERRA2GMI/). The training dataset and training targets for the
735 July parameterization presented here are available at <https://doi.org/10.5281/zenodo.6604130>
736 (Anderson, 2022b). Output from the GEOSCCM simulation for CCMI is available at the Centre for
737 Environmental Data Analysis (CED), the Natural Environment Research Council's Data Repository for
738 Atmospheric Science and Earth Observation, at [http://data.ceda.ac.uk/badc/wcrp-ccmi/data/CCMI-](http://data.ceda.ac.uk/badc/wcrp-ccmi/data/CCMI-1/output)
739 [1/output](http://data.ceda.ac.uk/badc/wcrp-ccmi/data/CCMI-1/output).

740

741 **7.0 Author Contributions**

742 DCA wrote the manuscript, performed the data analysis, and created the parameterizations. BND and
743 MBFC developed the idea for the parameterization. SAS performed three-dimensional modeling for the
744 work. JMN and PDI provided advice on machine learning. All authors helped develop ideas for the
745 analysis and contributed to the manuscript,

746

747 **8.0 Competing Interests**

748 The authors declare that they have no conflict of interest.

749

750 **9.0 Acknowledgements**

751 The authors acknowledge funding from the NASA MAP program (grant no. 80NSSC17K0220). In
752 addition, the authors acknowledge funding from the NASA Aura program.

753

754

10. References

755

756 Anderson, D. C., Duncan, B. N., Fiore, A. M., Baublitz, C. B., Follette-Cook, M. B., Nicely, J. M., and Wolfe,
757 G. M.: Spatial and temporal variability in the hydroxyl (OH) radical: understanding the role of large-scale
758 climate features and their influence on OH through its dynamical and photochemical drivers,
759 *Atmospheric Chemistry and Physics*, 21, 6481-6508, [10.5194/acp-21-6481-2021](https://doi.org/10.5194/acp-21-6481-2021), 2021.

760

761 Anderson, D.C., Follette-Cook, M.B., Strode, S.A., Nicely, J.M., Liu, J., Ivatt, P.D., Duncan, B.N. (2022a).

762 Code for the development of a parameterization of OH for CCMs, Zenodo[code],

<https://doi.org/10.5281/zenodo.6046037>.

763

764 Anderson, D.C., Follette-Cook, M.B., Strode, S.A., Nicely, J.M., Liu, J., Ivatt, P.D., & Duncan, B.N. (2022b)

Sample ECCOH OH Parameterization (1.0) [Data set]. Zenodo. <https://doi.org/10.5281/zenodo.6604130>.

765

766 Chen, T., and Guestrin, C.: XGBoost: A Scalable Tree Boosting System, KDD '16: Proceedings of the 22nd
ACM SIGKDD International Conference on Knowledge Discovery and Data Mining, 2016, 785-794.

767

768 Chen, Y.-H., and Prinn, R. G.: Estimation of atmospheric methane emissions between 1996 and 2001
769 using a three-dimensional global chemical transport model, *Journal of Geophysical Research:*

Atmospheres, 111, <https://doi.org/10.1029/2005JD006058>, 2006.

770

771 Chin, M., Ginoux, P., Kinne, S., Torres, O., Holben, B. N., Duncan, B. N., Martin, R. V., Logan, J. A.,

Higurashi, A., and Nakajima, T.: Tropospheric Aerosol Optical Thickness from the GOCART Model and

772 Comparisons with Satellite and Sun Photometer Measurements, *Journal of the Atmospheric Sciences*,
773 59, 461-483, 10.1175/1520-0469(2002)059<0461:TAOTFT>2.0.CO;2, 2002.

774 Colarco, P., da Silva, A., Chin, M., and Diehl, T.: Online simulations of global aerosol distributions in the
775 NASA GEOS-4 model and comparisons to satellite and ground-based aerosol optical depth, *Journal of*
776 *Geophysical Research: Atmospheres*, 115, <https://doi.org/10.1029/2009JD012820>, 2010.

777 Du, M., Huang, K., Zhang, S., Huang, C., Gong, Y., and Yi, F.: Water vapor anomaly over the tropical
778 western Pacific in El Niño winters from radiosonde and satellite observations and ERA5 reanalysis data,
779 *Atmos. Chem. Phys.*, 21, 13553-13569, 10.5194/acp-21-13553-2021, 2021.

780 Duncan, B., Portman, D., Bey, I., and Spivakovsky, C.: Parameterization of OH for efficient computation in
781 chemical tracer models, *Journal of Geophysical Research: Atmospheres*, 105, 12259-12262,
782 10.1029/1999JD901141, 2000.

783 Duncan, B. N.: Indonesian wildfires of 1997: Impact on tropospheric chemistry, *Journal of Geophysical*
784 *Research*, 108, 10.1029/2002jd003195, 2003a.

785 Duncan, B. N.: Interannual and seasonal variability of biomass burning emissions constrained by satellite
786 observations, *Journal of Geophysical Research*, 108, 10.1029/2002jd002378, 2003b.

787 Duncan, B. N., Logan, J. A., Bey, I., Megretskaia, I. A., Yantosca, R. M., Novelli, P. C., Jones, N. B., and
788 Rinsland, C. P.: Global budget of CO, 1988–1997: Source estimates and validation with a global model,
789 *Journal of Geophysical Research*, 112, 10.1029/2007jd008459, 2007a.

790 Duncan, B. N., Strahan, S. E., Yoshida, Y., Steenrod, S. D., and Livesey, N.: Model study of the cross-
791 tropopause transport of biomass burning pollution, *Atmos. Chem. Phys.*, 7, 3713-3736, 10.5194/acp-7-
792 3713-2007, 2007b.

793 Duncan, B. N., and Logan, J. A.: Model analysis of the factors regulating the trends and variability of
794 carbon monoxide between 1988 and 1997, *Atmospheric Chemistry and Physics*, 8, 2008.

795 Elith, J., Leathwick, J. R., and Hastie, T.: A working guide to boosted regression trees, *J Anim Ecol*, 77,
796 802-813, 10.1111/j.1365-2656.2008.01390.x, 2008.

797 Elshorbany, Y. F., Duncan, B. N., Strode, S. A., Wang, J. S., and Kouatchou, J.: The description and
798 validation of the computationally Efficient CH₄–CO–OH (ECCOHv1.01) chemistry module for 3-D model
799 applications, *Geoscientific Model Development*, 9, 799-822, 10.5194/gmd-9-799-2016, 2016.

800 Fiore, A. M., Horowitz, L. W., Dlugokencky, E. J., and West, J. J.: Impact of meteorology and emissions on
801 methane trends, 1990–2004, *Geophysical Research Letters*, 33, 10.1029/2006gl026199, 2006.

802 Gaubert, B., Worden, H. M., Arellano, A. F. J., Emmons, L. K., Tilmes, S., Barré, J., Martinez Alonso, S.,
803 Vitt, F., Anderson, J. L., Alkemade, F., Houweling, S., and Edwards, D. P.: Chemical Feedback From
804 Decreasing Carbon Monoxide Emissions, *Geophysical Research Letters*, 44, 9985-9995,
805 <https://doi.org/10.1002/2017GL074987>, 2017.

806 Gelaro, R., McCarty, W., Suarez, M. J., Todling, R., Molod, A., Takacs, L., Randles, C., Darmenov, A.,
807 Bosilovich, M. G., Reichle, R., Wargan, K., Coy, L., Cullather, R., Draper, C., Akella, S., Buchard, V., Conaty,

808 A., da Silva, A., Gu, W., Kim, G. K., Koster, R., Lucchesi, R., Merkova, D., Nielsen, J. E., Partyka, G.,
809 Pawson, S., Putman, W., Rienecker, M., Schubert, S. D., Sienkiewicz, M., and Zhao, B.: The Modern-Era
810 Retrospective Analysis for Research and Applications, Version 2 (MERRA-2), *J Clim*, Volume 30, 5419-
811 5454, 10.1175/JCLI-D-16-0758.1, 2017.

812 Holmes, C. D.: Methane Feedback on Atmospheric Chemistry: Methods, Models, and Mechanisms,
813 *Journal of Advances in Modeling Earth Systems*, 10, 1087-1099,
814 <https://doi.org/10.1002/2017MS001196>, 2018.

815 Ivatt, P. D., and Evans, M. J.: Improving the prediction of an atmospheric chemistry transport model
816 using gradient-boosted regression trees, *Atmospheric Chemistry and Physics*, 20, 8063-8082,
817 10.5194/acp-20-8063-2020, 2020.

818 Keller, C. A., and Evans, M. J.: Application of random forest regression to the calculation of gas-phase
819 chemistry within the GEOS-Chem chemistry model v10, *Geoscientific Model Development*, 12, 1209-
820 1225, 10.5194/gmd-12-1209-2019, 2019.

821 Kelp, M. M., Jacob, D. J., Kutz, J. N., Marshall, J. D., and Tessum, C. W.: Toward Stable, General Machine-
822 Learned Models of the Atmospheric Chemical System, *Journal of Geophysical Research: Atmospheres*,
823 125, e2020JD032759, <https://doi.org/10.1029/2020JD032759>, 2020.

824 Kleipool, Q. L., Dobber, M. R., de Haan, J. F., and Levelt, P. F.: Earth surface reflectance climatology from
825 3 years of OMI data, *Journal of Geophysical Research: Atmospheres*, 113,
826 <https://doi.org/10.1029/2008JD010290>, 2008.

827 Kug, J.-S., Jin, F.-F., and An, S.-I.: Two Types of El Niño Events: Cold Tongue El Niño and Warm Pool El
828 Niño, *Journal of Climate*, 22, 1499-1515, 10.1175/2008JCLI2624.1, 2009.

829 Laughner, J. L., Neu, J. L., Schimel, D., Wennberg, P. O., Barsanti, K., Bowman, K. W., Chatterjee, A.,
830 Croes, B. E., Fitzmaurice, H. L., Henze, D. K., Kim, J., Kort, E. A., Liu, Z., Miyazaki, K., Turner, A. J.,
831 Anenberg, S., Avise, J., Cao, H., Crisp, D., de Gouw, J., Eldering, A., Fyfe, J. C., Goldberg, D. L., Gurney, K.
832 R., Hasheminassab, S., Hopkins, F., Ivey, C. E., Jones, D. B. A., Liu, J., Lovenduski, N. S., Martin, R. V.,
833 McKinley, G. A., Ott, L., Poulter, B., Ru, M., Sander, S. P., Swart, N., Yung, Y. L., and Zeng, Z. C.: Societal
834 shifts due to COVID-19 reveal large-scale complexities and feedbacks between atmospheric chemistry
835 and climate change, *Proc Natl Acad Sci U S A*, 118, 10.1073/pnas.2109481118, 2021.

836 Lawrence, M. G., Jöckel, P., and von Kuhlmann, R.: What does the global mean OH concentration tell
837 us?, *Atmos. Chem. Phys.*, 1, 37-49, 10.5194/acp-1-37-2001, 2001.

838 Lundberg, S. M., and Lee, S.-I.: A Unified Approach to Interpreting Model Predictions, 31st Conference
839 on Neural Information Processing Systems, Long Beach, CA, USA, 2017.

840 Morgenstern, O., Hegglin, M. I., Rozanov, E., Connor, F. M., Abraham, N. L., Akiyoshi, H., Archibald, A. T.,
841 Bekki, S., Butchart, N., Chipperfield, M. P., Deushi, M., Dhomse, S. S., Garcia, R. R., Hardiman, S. C.,
842 Horowitz, L. W., Jöckel, P., Josse, B., Kinnison, D., Lin, M., Mancini, E., Manyin, M. E., Marchand, M.,
843 Marécal, V., Michou, M., Oman, L. D., Pitari, G., Plummer, D. A., Revell, L. E., Saint-Martin, D., Schofield,
844 R., Stenke, A., Stone, K., Sudo, K., Tanaka, T. Y., Tilmes, S., Yamashita, Y., Yoshida, K., and Zeng, G.:
845 Review of the global models used within phase 1 of the Chemistry–Climate Model Initiative (CCMI),
846 *Geoscientific Model Development*, 10, 639-671, 10.5194/gmd-10-639-2017, 2017.

847 Murray, L. T., Logan, J. A., and Jacob, D. J.: Interannual variability in tropical tropospheric ozone and OH:
848 The role of lightning, *Journal of Geophysical Research: Atmospheres*, 118, 11,468-411,480,
849 10.1002/jgrd.50857, 2013.

850 Murray, L. T., Mickley, L. J., Kaplan, J. O., Sofen, E. D., Pfeiffer, M., and Alexander, B.: Factors controlling
851 variability in the oxidative capacity of the troposphere since the Last Glacial Maximum, *Atmospheric*
852 *Chemistry and Physics*, 14, 3589-3622, 10.5194/acp-14-3589-2014, 2014.

853 Murray, L. T., Fiore, A. M., Shindell, D. T., Naik, V., and Horowitz, L. W.: Large uncertainties in global
854 hydroxyl projections tied to fate of reactive nitrogen and carbon, *Proceedings of the National Academy*
855 *of Sciences*, 118, e2115204118, 10.1073/pnas.2115204118, 2021.

856 Nicely, J. M., Salawitch, R. J., Canty, T., Anderson, D. C., Arnold, S. R., Chipperfield, M. P., Emmons, L. K.,
857 Flemming, J., Huijnen, V., Kinnison, D. E., Lamarque, J.-F., Mao, J., Monks, S. A., Steenrod, S. D., Tilmes,
858 S., and Turquety, S.: Quantifying the causes of differences in tropospheric OH within global models,
859 *Journal of Geophysical Research: Atmospheres*, n/a-n/a, 10.1002/2016JD026239, 2017.

860 Nicely, J. M., Duncan, B. N., Hanisco, T. F., Wolfe, G. M., Salawitch, R. J., Deushi, M., Haslerud, A. S.,
861 Jöckel, P., Josse, B., Kinnison, D. E., Klekociuk, A., Manyin, M. E., Marécal, V., Morgenstern, O., Murray, L.
862 T., Myhre, G., Oman, L. D., Pitari, G., Pozzer, A., Quaglia, I., Revell, L. E., Rozanov, E., Stenke, A., Stone, K.,
863 Strahan, S., Tilmes, S., Tost, H., Westervelt, D. M., and Zeng, G.: A machine learning examination of
864 hydroxyl radical differences among model simulations for CCMI-1, *Atmospheric Chemistry and Physics*,
865 20, 1341-1361, 10.5194/acp-20-1341-2020, 2020.

866 Nowack, P., Braesicke, P., Haigh, J., Abraham, N. L., Pyle, J., and Voulgarakis, A.: Using machine learning
867 to build temperature-based ozone parameterizations for climate sensitivity simulations, *Environmental*
868 *Research Letters*, 13, 104016, 10.1088/1748-9326/aae2be, 2018.

869 Nowack, P., Konstantinovskiy, L., Gardiner, H., and Cant, J.: Machine learning calibration of low-cost NO₂
870 and PM₁₀ sensors: non-linear algorithms and their impact on site transferability, *Atmos. Meas. Tech.*,
871 14, 5637-5655, 10.5194/amt-14-5637-2021, 2021.

872 Oman, L. D., Ziemke, J. R., Douglass, A. R., Waugh, D. W., Lang, C., Rodriguez, J. M., and Nielsen, J. E.: The
873 response of tropical tropospheric ozone to ENSO, *Geophysical Research Letters*, 38, n/a-n/a,
874 10.1029/2011gl047865, 2011.

875 Oman, L. D., Douglass, A. R., Ziemke, J. R., Rodriguez, J. M., Waugh, D. W., and Nielsen, J. E.: The ozone
876 response to ENSO in Aura satellite measurements and a chemistry-climate simulation, *Journal of*
877 *Geophysical Research-Atmospheres*, 118, 965-976, 10.1029/2012jd018546, 2013.

878 Orbe, C., Oman, L. D., Strahan, S. E., Waugh, D. W., Pawson, S., Takacs, L. L., and Molod, A. M.: Large-
879 Scale Atmospheric Transport in GEOS Replay Simulations, *Journal of Advances in Modeling Earth*
880 *Systems*, 9, 2545-2560, 10.1002/2017ms001053, 2017.

881 Paek, H., Yu, J.-Y., and Qian, C.: Why were the 2015/2016 and 1997/1998 extreme El Niños different?,
882 *Geophysical Research Letters*, 44, 1848-1856, <https://doi.org/10.1002/2016GL071515>, 2017.

883 Prather, M. J.: Time scales in atmospheric chemistry: Theory, GWPs for CH₄ and CO, and runaway
884 growth, *Geophysical Research Letters*, 23, 2597-2600, <https://doi.org/10.1029/96GL02371>, 1996.

885 Rigby, M., Montzka, S. A., Prinn, R. G., White, J. W. C., Young, D., O'Doherty, S., Lunt, M. F., Ganesan, A.
886 L., Manning, A. J., Simmonds, P. G., Salameh, P. K., Harth, C. M., Muhle, J., Weiss, R. F., Fraser, P. J.,
887 Steele, L. P., Krummel, P. B., McCulloch, A., and Park, S.: Role of atmospheric oxidation in recent
888 methane growth, *Proc Natl Acad Sci U S A*, 114, 5373-5377, [10.1073/pnas.1616426114](https://doi.org/10.1073/pnas.1616426114), 2017.

889 Rowlinson, M. J., Rap, A., Arnold, S. R., Pope, R. J., Chipperfield, M. P., McNorton, J., Forster, P., Gordon,
890 H., Pringle, K. J., Feng, W., Kerridge, B. J., Latter, B. L., and Siddans, R.: Impact of El Niño–Southern
891 Oscillation on the interannual variability of methane and tropospheric ozone, *Atmospheric Chemistry
892 and Physics*, 19, 8669-8686, [10.5194/acp-19-8669-2019](https://doi.org/10.5194/acp-19-8669-2019), 2019.

893 Saito, R., Patra, P. K., Sweeney, C., Machida, T., Krol, M., Houweling, S., Bousquet, P., Agusti-Panareda,
894 A., Belikov, D., Bergmann, D., Bian, H., Cameron-Smith, P., Chipperfield, M. P., Fortems-Cheiney, A.,
895 Fraser, A., Gatti, L. V., Gloor, E., Hess, P., Kawa, S. R., Law, R. M., Locatelli, R., Loh, Z., Maksyutov, S.,
896 Meng, L., Miller, J. B., Palmer, P. I., Prinn, R. G., Rigby, M., and Wilson, C.: TransCom model simulations
897 of methane: Comparison of vertical profiles with aircraft measurements, *Journal of Geophysical
898 Research: Atmospheres*, 118, 3891-3904, <https://doi.org/10.1002/jgrd.50380>, 2013.

899 Shapley, L. S.: A Value for N-Person Games, in: *Contributions to the Theory of Games*, edited by: Kuhn,
900 H. W., and Tucker, A. W., *Ann. Math. Studies*, 28, Princeton University Press, 307-317, 1953.

901 Sherwen, T., Chance, R. J., Tinel, L., Ellis, D., Evans, M. J., and Carpenter, L. J.: A machine-learning-based
902 global sea-surface iodide distribution, *Earth Syst. Sci. Data*, 11, 1239-1262, [10.5194/essd-11-1239-2019](https://doi.org/10.5194/essd-11-1239-2019),
903 2019.

904 Shi, L., Schreck, C., and Schröder, M.: Assessing the Pattern Differences between Satellite-Observed
905 Upper Tropospheric Humidity and Total Column Water Vapor during Major El Niño Events, *Remote
906 Sensing*, 10, [10.3390/rs10081188](https://doi.org/10.3390/rs10081188), 2018.

907 Spivakovsky, C. M., Wofsy, S. C., and Prather, M. J.: A numerical method for parameterization of
908 atmospheric chemistry: Computation of tropospheric OH, *Journal of Geophysical Research:
909 Atmospheres*, 95, 18433-18439, <https://doi.org/10.1029/JD095iD11p18433>, 1990.

910 Spivakovsky, C. M., Logan, J. A., Montzka, S. A., Balkanski, Y. J., Foreman-Fowler, M., Jones, D. B. A.,
911 Horowitz, L. W., Fusco, A. C., Brenninkmeijer, C. A. M., Prather, M. J., Wofsy, S. C., and McElroy, M. B.:
912 Three-dimensional climatological distribution of tropospheric OH: Update and evaluation, *Journal of
913 Geophysical Research: Atmospheres*, 105, 8931-8980, [10.1029/1999jd901006](https://doi.org/10.1029/1999jd901006), 2000.

914 Stirnberg, R., Cermak, J., Fuchs, J., and Andersen, H.: Mapping and Understanding Patterns of Air Quality
915 Using Satellite Data and Machine Learning, *Journal of Geophysical Research: Atmospheres*, 125,
916 [e2019JD031380](https://doi.org/10.1029/2019JD031380), [10.1029/2019JD031380](https://doi.org/10.1029/2019JD031380), 2020.

917 Strahan, S. E., Duncan, B. N., and Hoor, P.: Observationally derived transport diagnostics for the
918 lowermost stratosphere and their application to the GMI chemistry and transport model, *Atmos. Chem.
919 Phys.*, 7, 2435-2445, [10.5194/acp-7-2435-2007](https://doi.org/10.5194/acp-7-2435-2007), 2007.

920 Strobe, S. A., Duncan, B. N., Yegorova, E. A., Kouatchou, J., Ziemke, J. R., and Douglass, A. R.: Implications
921 of carbon monoxide bias for methane lifetime and atmospheric composition in chemistry climate
922 models, *Atmospheric Chemistry and Physics*, 15, 11789-11805, [10.5194/acp-15-11789-2015](https://doi.org/10.5194/acp-15-11789-2015), 2015.

923 Strode, S. A., Ziemke, J. R., Oman, L. D., Lamsal, L. N., Olsen, M. A., and Liu, J.: Global changes in the
924 diurnal cycle of surface ozone, *Atmospheric Environment*, 199, 323-333,
925 10.1016/j.atmosenv.2018.11.028, 2019.

926 Turner, A. J., Frankenberg, C., Wennberg, P. O., and Jacob, D. J.: Ambiguity in the causes for decadal
927 trends in atmospheric methane and hydroxyl, *Proceedings of the National Academy of Sciences*, 114,
928 5367, 10.1073/pnas.1616020114, 2017.

929 Turner, A. J., Fung, I., Naik, V., Horowitz, L. W., and Cohen, R. C.: Modulation of hydroxyl variability by
930 ENSO in the absence of external forcing, *Proc Natl Acad Sci U S A*, 115, 8931-8936,
931 10.1073/pnas.1807532115, 2018.

932 Voulgarakis, A., Naik, V., Lamarque, J. F., Shindell, D. T., Young, P. J., Prather, M. J., Wild, O., Field, R. D.,
933 Bergmann, D., Cameron-Smith, P., Cionni, I., Collins, W. J., Dalsøren, S. B., Doherty, R. M., Eyring, V.,
934 Faluvegi, G., Folberth, G. A., Horowitz, L. W., Josse, B., MacKenzie, I. A., Nagashima, T., Plummer, D. A.,
935 Righi, M., Rumbold, S. T., Stevenson, D. S., Strode, S. A., Sudo, K., Szopa, S., and Zeng, G.: Analysis of
936 present day and future OH and methane lifetime in the ACCMIP simulations, *Atmospheric Chemistry and
937 Physics*, 13, 2563-2587, 10.5194/acp-13-2563-2013, 2013.

938 Voulgarakis, A., Marlier, M. E., Faluvegi, G., Shindell, D. T., Tsigaridis, K., and Mangeon, S.: Interannual
939 variability of tropospheric trace gases and aerosols: The role of biomass burning emissions, *Journal of
940 Geophysical Research: Atmospheres*, 120, 7157-7173, 10.1002/2014jd022926, 2015.

941 Wang, J. S., Logan, J. A., McElroy, M. B., Duncan, B. N., Megretskaya, I. A., and Yantosca, R. M.: A 3-D
942 model analysis of the slowdown and interannual variability in the methane growth rate from 1988 to
943 1997, *Global Biogeochemical Cycles*, 18, <https://doi.org/10.1029/2003GB002180>, 2004.

944 Wolfe, G. M., Nicely, J. M., St Clair, J. M., Hanisco, T. F., Liao, J., Oman, L. D., Brune, W. B., Miller, D.,
945 Thames, A., Gonzalez Abad, G., Ryerson, T. B., Thompson, C. R., Peischl, J., McCain, K., Sweeney, C.,
946 Wennberg, P. O., Kim, M., Crouse, J. D., Hall, S. R., Ullmann, K., Diskin, G., Bui, P., Chang, C., and Dean-
947 Day, J.: Mapping hydroxyl variability throughout the global remote troposphere via synthesis of airborne
948 and satellite formaldehyde observations, *Proc Natl Acad Sci U S A*, 116, 11171-11180,
949 10.1073/pnas.1821661116, 2019.

950 Wolter, K., and Timlin, M. S.: El Niño/Southern Oscillation behaviour since 1871 as diagnosed in an
951 extended multivariate ENSO index (MEI.ext), *International Journal of Climatology*, 31, 1074-1087,
952 10.1002/joc.2336, 2011.

953 Worden, J., Jiang, Z., Jones, D. B. A., Alvarado, M., Bowman, K., Frankenberg, C., Kort, E. A., Kulawik, S.
954 S., Lee, M., Liu, J., Payne, V., Wecht, K., and Worden, H.: El Niño, the 2006 Indonesian peat fires, and the
955 distribution of atmospheric methane, *Geophysical Research Letters*, 40, 4938-4943,
956 <https://doi.org/10.1002/grl.50937>, 2013.

957 Yan, R., Ma, Z., Zhao, Y., and Kokogiannakis, G.: A decision tree based data-driven diagnostic strategy for
958 air handling units, *Energy and Buildings*, 133, 37-45, <https://doi.org/10.1016/j.enbuild.2016.09.039>,
959 2016.

- 960 Zhang, Z., Zimmermann, N. E., Calle, L., Hurtt, G., Chatterjee, A., and Poulter, B.: Enhanced response of
961 global wetland methane emissions to the 2015–2016 El Niño-Southern Oscillation event, *Environmental*
962 *Research Letters*, 13, 10.1088/1748-9326/aac939, 2018.
- 963 Zhu, Q., Laughner, J. L., and Cohen, R. C.: Combining Machine Learning and Satellite Observations to
964 Predict Spatial and Temporal Variation of near Surface OH in North American Cities, *Environmental*
965 *Science & Technology*, 10.1021/acs.est.1c05636, 2022.
- 966